Journal of Geophysical Research: Atmospheres

RESEARCH ARTICLE
10.1029/2017JD028043

Impact of Boreal Summer Intraseasonal Oscillation on Rainfall Extremes in Southeastern China and its Predictability in CFSv2

Pengfei Ren[1,2], Hong-Li Ren[2,3], Joshua-Xiouhua Fu[4], Jie Wu[2], and Liangmin Du[5]

[1]Chinese Academy of Meteorological Sciences, Beijing, China, [2]Laboratory for Climate Studies, CMA-NJU Joint Laboratory for Climate Prediction Studies, National Climate Center, China Meteorological Administration, Beijing, China, [3]Department of Atmospheric Sciences, School of Environment Studies University of Geoscience, Wuhan, China, [4]Institute of Atmospheric Sciences, Fudan University, Shanghai, China, [5]Wuhan Regional Climate Center, Hubei, China

Key Points:
- BSISO significantly influences probability of extreme rainfall in southeastern China, showing an evident regional dependence
- Intensified moisture convergence and upward moisture transport during BSISO active phases favor the occurrence of extreme rainfall
- CFSv2 can well reproduce the impact of BSISO on extreme rainfall and show considerable predictability

Correspondence to:
H.-L. Ren,
renhl@cma.gov.cn

Citation:
Ren, P., Ren, H.-L., Fu, J.-X., Wu, J., & Du, L. (2018). Impact of boreal summer intraseasonal oscillation on rainfall extremes in southeastern China and its predictability in CFSv2. *Journal of Geophysical Research: Atmospheres*, *123*, 4423–4442. https://doi.org/10.1029/2017JD028043

Received 10 NOV 2017
Accepted 27 MAR 2018
Accepted article online 12 APR 2018
Published online 2 MAY 2018

Abstract The boreal summer intraseasonal oscillation (BSISO) is one of the dominant modes of intraseasonal variability of the tropical climate system, which has prominent northward propagation extending much further from the equator. The impacts of BSISO on extreme rainfall in eastern China were studied using the BSISO indices and daily rainfall data in China. We revealed that the responses of extreme rainfall to BSISO activity in eastern China are not spatially uniform. Under the influences of BSISO1, the probability-distribution functions of rainfall in two southeastern China subregions: South China and Yangtze River Valley significantly skew toward larger values, respectively, in phases 4 and 8, and phases 3 and 4 with the probability of 90th extremes increased by 35–45% relative to May–August rainfall probability-distribution function, showing southward propagation with the speed of 1.96°/phase. Under the BSISO2, the probability of the 90th extremes increased more than 40% in South China and Yangtze River Valley, respectively, during phases 4–5 and phases 6–7, showing northward propagation with a speed of 2.75°/phase. Physical analysis showed that the increased probability of extreme rainfall is associated with intensifying moisture convergence and upward moisture transport during BSISO active phases. The hindcasts from the Climate Forecast System version 2 have been used to evaluate the modulations of BSISO on extreme rainfall and associated predictability. It was shown that the Climate Forecast System version well reproduces the modulations of BSISO on extreme rainfall within 2 weeks. These results demonstrate the feasibility to develop medium-to-extended-range probabilistic forecasts of extreme rainfall for southeastern China.

1. Introduction

Extreme rainfall is one of the most prominent extreme weather and climate events. Its sudden and destructive characteristics can lead to flood, landslide, and mudflow with the potential to cause catastrophic losses of property, agriculture, and even threaten the human lives. In the summer of 1998, a major flood that occurred in Yangtze River Valley (YRV) claimed over 3,000 lives and resulted in $45 billion economic loss (Huang et al., 1998). In May–June of 2008, the persistent heavy rainfall over South China (SC) caused 168 people dead (Wang et al., 2011). In June of 2010, 15 consecutive days of heavy rain in Fujian Province affected more than 2.95 million people's lives and caused direct economic losses up to $1.6 billion (Gao et al., 2013). Due to high vulnerability to rainfall extremes in eastern China (EC), better understanding the physical processes inducing prolonged heavy rainfall and improving prediction skill for such extreme events are needed to establish an extended-range (10–30 days) flood forecast system and provide improved meteorological services for this region (Hsu et al., 2016; Lee et al., 2017; Webster et al., 2010).

One major source of predictability at the subseasonal-to-seasonal time range comes from the intraseasonal oscillation (ISO), especially the Madden-Julian Oscillation (MJO) characterized by a zonal planetary scale with eastward propagation occurs at a rate of about 5 m/s (Madden & Julian, 1971, 1972). As the leading mode of subseasonal variability in the tropical climate system, MJO can exert a significant impact on precipitation and temperature in different parts of the globe (Alvarez et al., 2016; Barlow et al., 2005; Bond & Vecchi, 2003; Jeong et al., 2005; Jia et al., 2011; Jones, 2000; Jones et al., 2004; Xavier et al., 2014; Zhang et al., 2009). However, the tropical ISO exhibits remarkable seasonal variations (Madden & Julian, 1994; Wang & Rui, 1990; Zhang & Dong, 2004). During boreal winter, MJO tends to be more active with stronger amplitude and more eastward-propagating events than other seasons, whereas it tends to be weaker during boreal summer. Compared to the equatorial-trapped eastward propagating MJO, the boreal summer ISO (BSISO) is more complex in nature with dominant northward propagation confined to the Indian and western

Pacific monsoon regions (Jiang et al., 2004; Lee et al., 2012). The BSISO is one of the key factors modulating the rainfall variability and flooding in the Asian monsoon regions (Chen et al., 2015; Hsu et al., 2016; Lee et al., 2017; Mao & Wu, 2006; Yang et al., 2010; Zhu et al., 2003).

In order to facilitate detection, monitoring, and prediction of the BSISO activity, Lee et al. (2012) proposed two BSISO indices based on multivariate empirical orthogonal function (EOF) analysis of daily anomalies of outgoing longwave radiation and 850-hPa zonal wind (U850) over the Asian monsoon sector (10°S–40°N, 40°E–160°E). The first two leading EOF modes, which together represent the canonical northward/northeastward propagating variability with quasi-oscillating periods of 30–60 days, are referred to as BSISO1. The other component referred to as BSISO2 is defined by the third and fourth EOF modes, which identify the 10 to 30-day northward/northwestward propagating variability. Recently, Hsu et al. (2016) used the BSISO indices to examine the influences of BSISO modes on the spatial distribution of extreme rainfall in southern China. Their results showed that the probability of extreme-rainfall events exceeding the 75th and 90th percentile can be significantly increased during the phases 2–4 of BSISO1 and the phases 5–7 of BSISO2 compared to the non-BSISO mode. However, the response of extreme rainfall to BSISO activity is not spatially uniform in the EC. What are the regional differences in the impact of BSISO on extreme rainfall in the EC and what are the underlying causes? This study will address these two questions.

As an important factor modulating weather activity, the predictability and prediction skill of BSISO is one of the key issues for extended-range forecasting. Fu et al. (2013) used four state-of-the-art models to evaluate the BSISO forecast skill. Their results showed that the intraseasonal forecast skills of the BSISO-related rainfall and zonal wind are, respectively, about 1–2 and 3 weeks measured with the spatial anomaly correlation coefficient (ACC). Zhao et al. (2014) assessed the performance of four Chinese AGCMs participating in the Coupled Model Intercomparison Project Phase 5 in the simulation of BSISO, and the results showed that the four models can reproduce boreal summer intraseasonal signals of precipitation. Lee et al. (2015) used six coupled models in the Intraseasonal Variability Hindcast Experiment project to examine the predictability and prediction skill of BSISO. They found that the multimodel-mean BSISO predictability and prediction skill with strong initial amplitude are about 45 and 22 days, respectively. Skillful prediction of BSISO offers an opportunity for probabilistic prediction of extreme rainfall in southeastern China (SEC) where BSISO has a significant impact. And from a prediction perspective, it would be useful to provide the probability information of extreme-rainfall events based on BSISO activity. Xavier et al. (2014) presented one method to evaluate the predictability of extreme-rainfall probability in Southeast Asia based on hindcasts from the operational GloSea5 forecasting system in the Met Office's Hadley Center. Their results demonstrated that it is feasible to derive probabilistic information about extreme-rainfall events at medium range during the passage of MJO. In the present study, we have also worked to explore the performance of one state-of-the-art operational Climate Forecast System version 2 (CFSv2) for forecasting the relationship between the BSISO and extreme rainfall, with the aim of assessing predictability of the extended-range probability of extreme-rainfall events in SEC.

The remainder of this paper is organized as follows: The data and methodology are given in section 2; section 3 presents the influences of BSISO on summer extreme rainfall in EC; furthermore, the physical basis for modulations of BSISO on rainfall extremes is briefly analyzed in order to illustrate the potential indicators of extreme events; then, evaluation of CFSv2's ability to forecast the relationship between the BSISO and extreme rainfall is presented in section 4; and summary and discussion are presented in section 5.

2. Data and Methods

2.1. Observational Data

The observational data used in this study include (1) daily rainfall from 2,400 stations in China covering the period from 1 January 1981 to 31 December 2013, as collected and compiled by the National Meteorological Information Center of the China Meteorological Administration; (2) NCEP-NCAR daily reanalysis (Kalnay et al., 1996), including wind, vertical velocity, and specific humidity covering the same period as the rainfall data; and (3) the BSISO index proposed by Lee et al. (2012), which was downloaded from http://www.apcc21.org/ser/moni.do?lang=en. Lee et al. (2012) demonstrated that the two

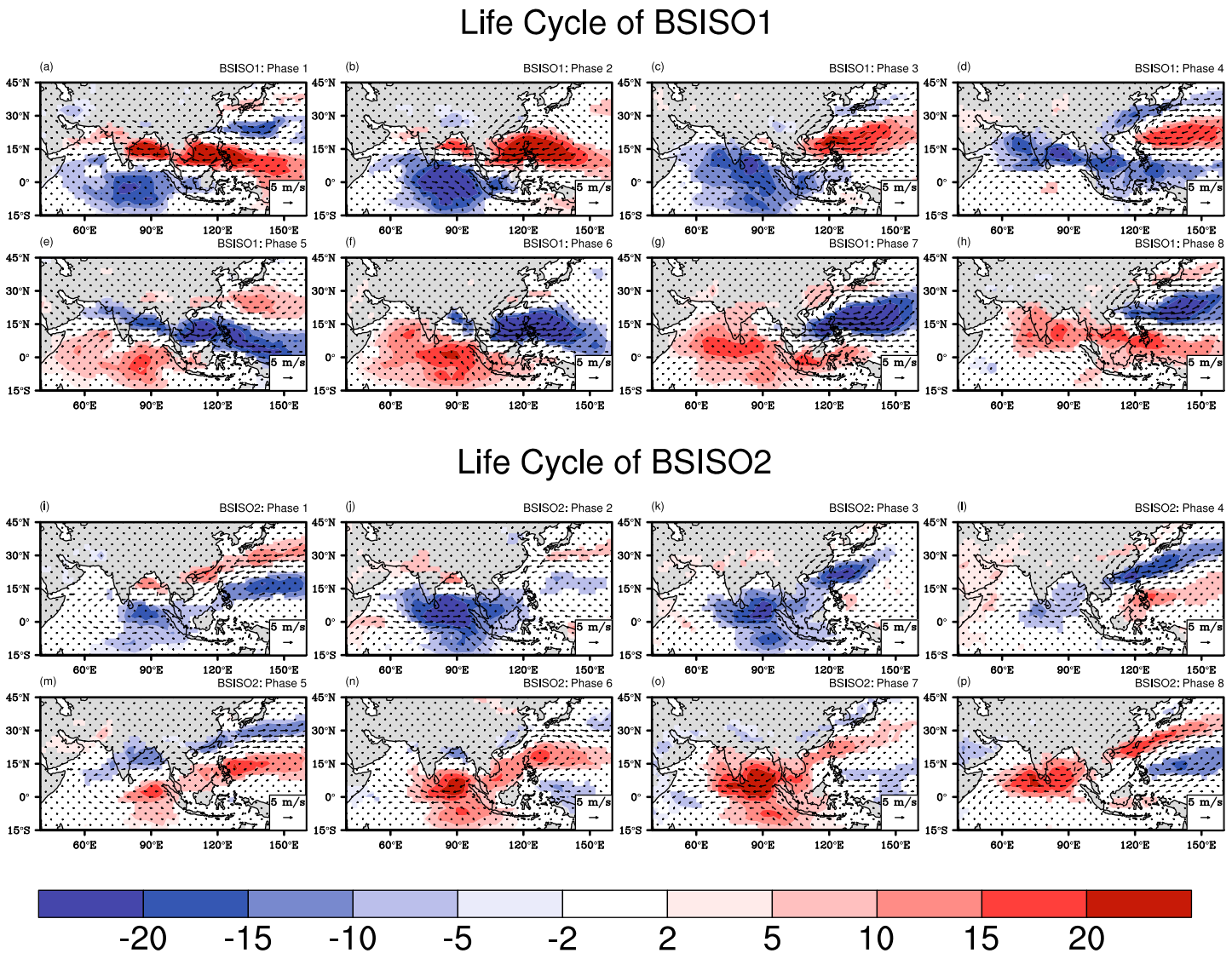

Figure 1. Life cycle composite of outgoing longwave radiation (OLR; shading) and 850-hPa wind (vector) anomaly based on eight phases of (a)–(h) boreal summer intraseasonal oscillation 1 and (i)–(p) boreal summer intraseasonal oscillation 2. Only 95% significant values are shaded for the OLR anomaly.

BSISO indices are capable of describing a large fraction of the total intraseasonal variability in Asia and better represent the northward propagation than the real-time multivariate MJO index (Wheeler & Hendon, 2004).

2.2. Forecast Data

Our analysis is based on the hindcasts from CFSv2 (Saha et al., 2010, 2014), which consists of fully coupled components of ocean, atmosphere and land. The atmospheric component is the NCEP Global Forecast System operational with a horizontal resolution of T126 (~100 km) and 64 vertical levels extending from the surface to 0.26 hPa. The oceanic component is the Geophysical Fluid Dynamics Laboratory Modular Ocean Model version 4, which uses 40 levels in the vertical direction, a zonal resolution of 0.5°, and a meridional resolution of 0.25° between 10°S and 10°N, gradually increasing through the tropics until becoming fixed at 0.5° poleward of 30°S and 30°N. Ren and Ren (2017) examined the model-based predictability for extreme rainfall in winter using hindcasts from CFSv2, and the results showed that the modulations of MJO on extreme rainfall are captured and forecasted well in the CFSv2 system. Adopting a similar approach, we

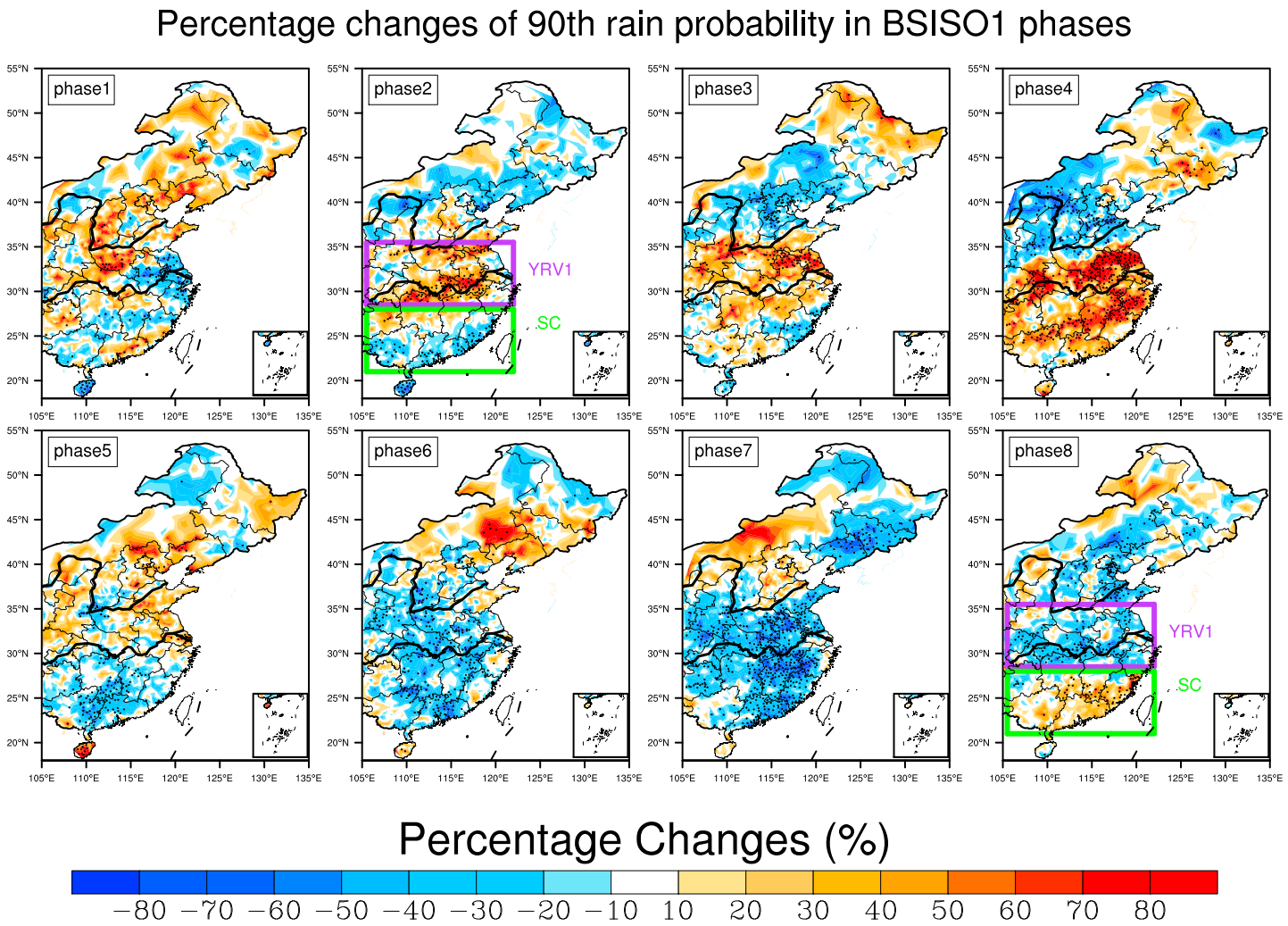

Figure 2. Percentage changes in the probability of rainfall at 90th extremes for each of eight phases of boreal summer intraseasonal oscillation 1. The dots represent stations that exceed the 95% confidence level. The Yangtze River Valley 1 and South China were selected by the purple and green boxes, respectively.

analyzed the 45-day hindcasts of CFSv2 initialized daily from 1 January 1999 to 31 December 2010. For each initial day, four forecasts were made every 6 hr at 00Z, 06Z, 12Z, and 18Z, forming a daily four-member ensemble mean.

2.3. Methods

The eight phases of BSISO1 (or BSISO2) were defined based on the signs and amplitudes of PC1 (PC3) and PC2 (PC4) (Lee et al., 2012) to show the evolutions and propagation features of BSISO. BSISO composites are constructed for BSISO1 and BSISO2 phases 1–8 with normalized amplitude greater than 1. General features of BSISO evolution are as follows (Figure 1): Convection anomaly associated with BSISO1 appears over the equatorial Indian Ocean in phase 1, and then propagates northeastward reaching the Indian subcontinent in phase 3 and the Bay of Bengal in phases 4 and 5. Then, convection anomaly over the Maritime Continent and equatorial western Pacific propagates northward and reaches the SC Sea in phase 7 and the WNP in phase 8. For BSISO2, the convection anomaly is located in the equatorial Indian Ocean and Philippine Sea in phase 1. Then, it propagates northwestward over the Indian Ocean and WNP-East Asian regions. For further details of the BSISO indices, the readers can referred to Lee et al. (2012).

Besides, following the percentile-based threshold method of Zhang et al. (2011), an extreme event was defined by a daily rainfall amount greater than the 90th (95th) percentile of the rainy days, which is

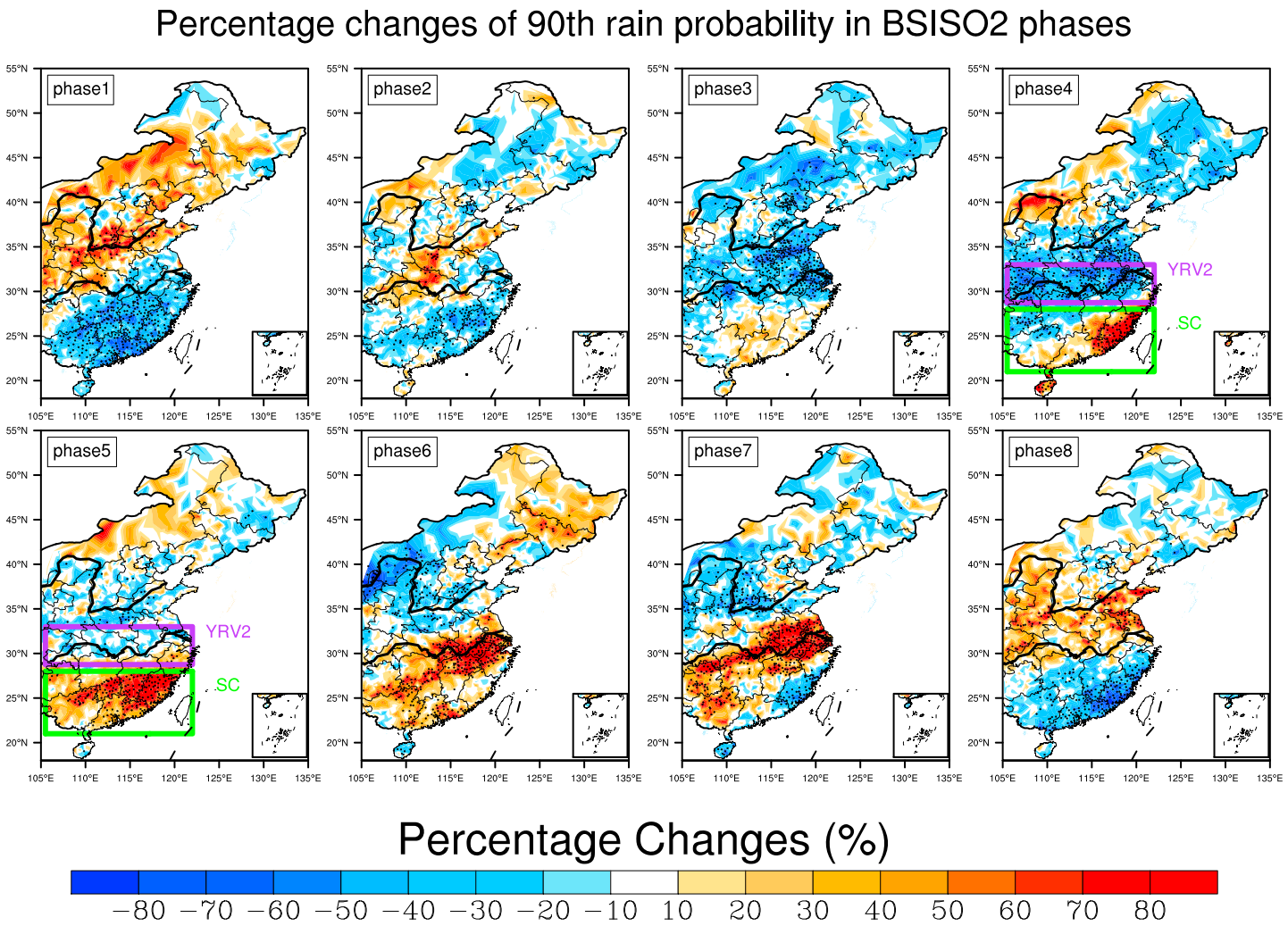

Figure 3. Same as Figure 2 but for each of eight phases of BSISO2.

referred to as the 90th (95th) extremes. Moreover, the percentage changes in probability-distribution functions (PDFs) of rainfall are calculated as follows:

$$\Delta P_{BSISO} = \frac{P_{BSISO}(x \geq x_c) - P_{all}(x \geq x_c)}{p_{all}(x \geq x_c)} \times 100\% \quad (1)$$

Here ΔP_{BSISO} is the percentage change in the cumulative probability of rainfall (x) exceeding a given threshold (x_c) due to the BSISO. P_{BSISO} is the cumulative probability that the rainfall exceeding the threshold calculated for only the days of the given BSISO1 (or BSISO2) phase, and P_{all} is for all days during the summer season.

The common period for all data sets (except for CFSv2 model) mentioned above covers the period from 1981 to 2013. Due to the data availability of CFSv2, the predictability of extreme rainfall was assessed only for the period from 1999 to 2010. The summer season in this paper was defined as the period from 1 May to 31 August (MJJA).

3. The Influences of BSISO on Extreme Rainfall

3.1. Modulations of BSISO on Rainfall Extremes

The composites of percentage change in the probability of rainfall at 90th extremes during BSISO1 phases 1–8 are shown in Figure 2. In order to better illustrate the regional differences in the impact

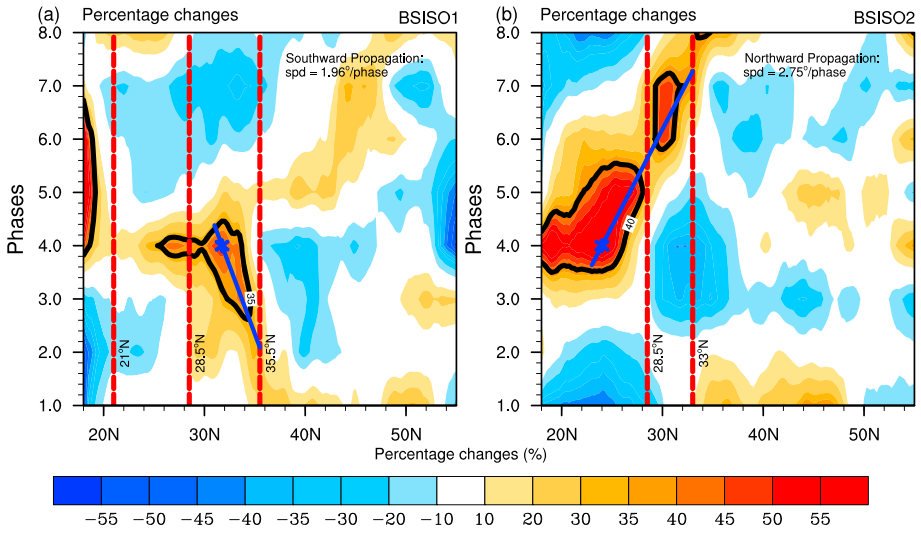

Figure 4. Zonal mean percentage changes in the probability of 90th extremes as a function of the eight phases of (a) boreal summer intraseasonal oscillation 1 and (b) boreal summer intraseasonal oscillation 2. The black-thick contours represent the increased probability of (a) 35% and (b) 40%. The blue-thick lines represent the percentage changes track and the slopes are defined as their (a) southward and (b) northward propagation speed.

of BSISO1 on extreme rainfall, we have shown the results in the entire EC region (e.g., east of 105°E). From Figure 2, we can clearly see that the probabilities of extreme rainfall in EC show systemic variations with the changes of BSISO1 phases. In general, significant changes in the probability of extreme rainfall are concentrated in the SEC. Given that the impact of BSISO1 on extreme rainfall is more significant in the SEC, we are going to focus on this region in the next research on the modulation of BSISO1 on extreme rainfall. The results of Figure 2 show that during the BSISO1 phases 2 and 3, the probabilities of 90th extremes increase in the YRV with a magnitude of more than 60% but decrease in northern and southern China. Only at the BSISO1 phase 4, the increases in probability of 90th extremes extend southward to cover almost the entire SEC region. Thus, the response of extreme rainfall to BSISO1 in the EC region is not always uniform. In fact, a dipole pattern between SC and YRV can be clearly seen in the BSISO1 phase 2 and phase 8. Due to the regional differences in the impact of BSISO1 on extreme rainfall, the SEC can be divided into two parts, namely, the SC (21°N–29.5°N) and YRV1 (29.5°N–35°N) regions (box in the Figure 2). Like BSISO1, we also investigated the impacts of BSISO2 on extreme rainfall in EC. Figure 3 shows the composite analysis similar to Figure 2, but for the phases 1–8 of BSISO2. In general, the modifications of BSISO2 on extreme rainfall are vigorous and the significant changes of 90th extremes are also concentrated in the SEC region. Similarly, the impacts of BSISO2 on extreme rainfall also show regional differences. For example, at BSISO2 phase 4 and phase 5, the frequency of extreme occurrence is significantly increased in the SC but reduced in the YRV. Moreover, it is interesting to note that the regional increases of extreme rainfall have steady northward propagation from southeastern coast to the north of the YRV during phases 4–8 (Hsu et al., 2016) and further toward northern China at phase 1. Similarly, the SEC can be divided into two parts, namely, SC (21°N -28.5°N) and the YRV2 (28.5°N–33°N; box in the Figure 3), based on the differences in the regional influences of BSISO2.

The regional differences mentioned above remind us that the spatial variations should be considered when investigating the impacts of BSISO on extreme rainfall in the EC. In order to better illustrate the meridional differences of BSISO modulations on rainfall extremes, the zonal mean percentage changes (calculated by east of 105°E) as a function of BSISO1 (or BSISO2) phases are given in Figure 4. From Figure 4a, we can clearly see that the typical active phases for the 90th extreme occurrences are phases 4 and 8 and phases 3 and 4, respectively, in SC and YRV1. During the typical active phases, the probabilities increase by more than 35% of 90th extremes. Besides, the regional increases of 90th extremes have a southward progression tendency during the BSISO1 phases 2–4. Following the approach of Ling et al. (2014), we can obtain the southward propagation speed of the modulations of BSISO1 on extreme rainfall based on this phase-latitude diagram

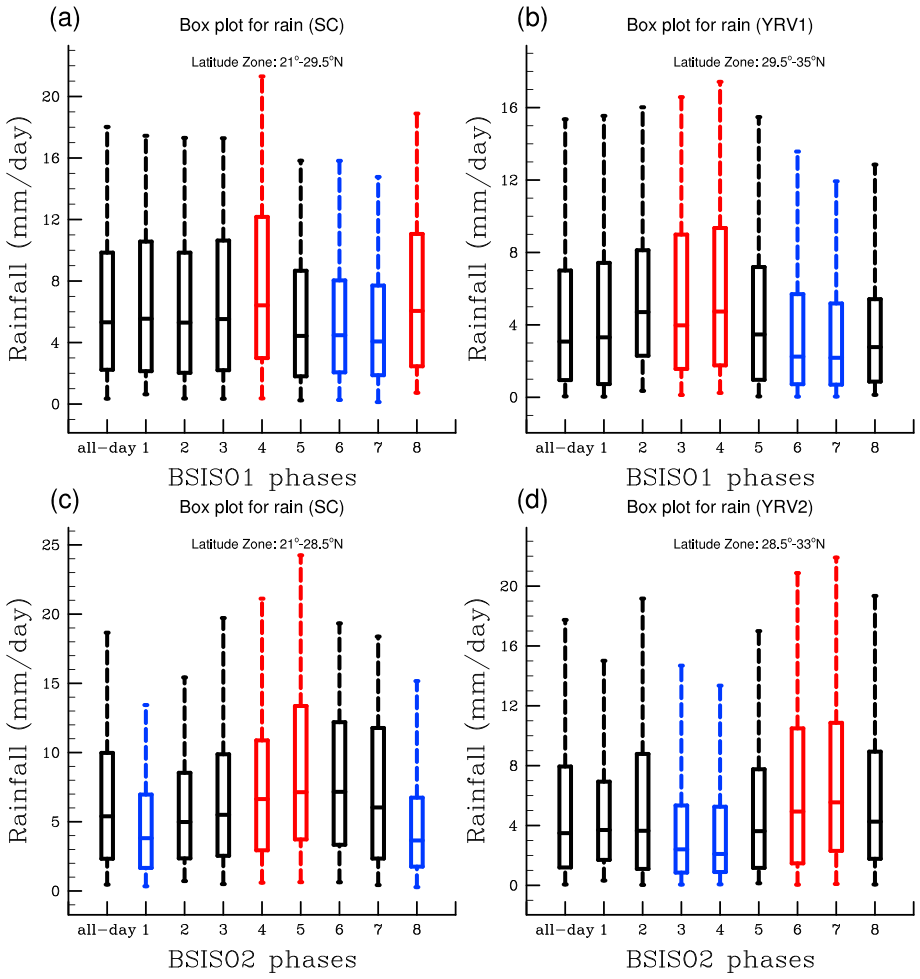

Figure 5. (a and b) Probability-distribution functions of rainfall averaged in a given area during boreal summer intraseasonal oscillation 1 phases 1–8 and all days (MJJA). (c and d) The same as (a) and (b) but for boreal summer intraseasonal oscillation 2 phases 1–8. The phases with a more positively (negatively) skewed distribution are in red (blue).

(Figure 4a). During the phases 2–4 of BSISO1, the typical speed for the southward propagation is about 1.96°/phase. Figure 4b shows the zonal mean percentage changes in the probability of 90th extremes as a function of the eight phases of BSISO2. From Figure 4b, we can see that the favorable phases for the 90th occurrence are phases 4–7 of BSISO2. Moreover, during these phases, the impacts of BSISO2 on 90th extremes have an obvious northward propagation with a speed of 2.75°/phase. This northward impact is closely related to the northwestward-propagating feature of BSISO2 mode in EC (Figure 9). On its course northward, the BSISO2 induces a dipole response of extreme rainfall in SC and YRV2. During phases 4–5 (6–7) of BSISO2, the probabilities of 90th extremes increase more than 40% (decrease) in SC and decrease (increase more than 40%) in the YRV2.

The changes in PDF of rainfall during BSISO1 and BSISO2 phases 1–8 with respect to the climatological PDF (with all days in MJJA included) are shown in Figure 5. The PDFs are obtained by selecting a given percentile for average rainfall over SC and YRV regions and represented as box plots with values for the 5th (lower bound), 25th (lower quartile), 50th (median), 75th (upper quartile), and 95th (upper bound) percentiles of the regional mean. We can define a selection criterion that separates more positively (negatively) skewed distributions and others by picking the top (lowest) two rainfall bins in the BSISOs' eight phases based on the 95th percentile rainfall. From Figures 5a and 5b, it can be seen that BSISO1 phases 4 and 8 and phases 3 and 4 tend to have a more positively skewed distribution compared to the climatological PDF in the SC and YRV1, respectively. In addition, BSISO1 phases 6 and 7 have a lower skewness of the PDF in SEC. The PDFs of rainfall during the phases 1–8 of BSISO2 are shown in Figures 5c and 5d. As mentioned above,

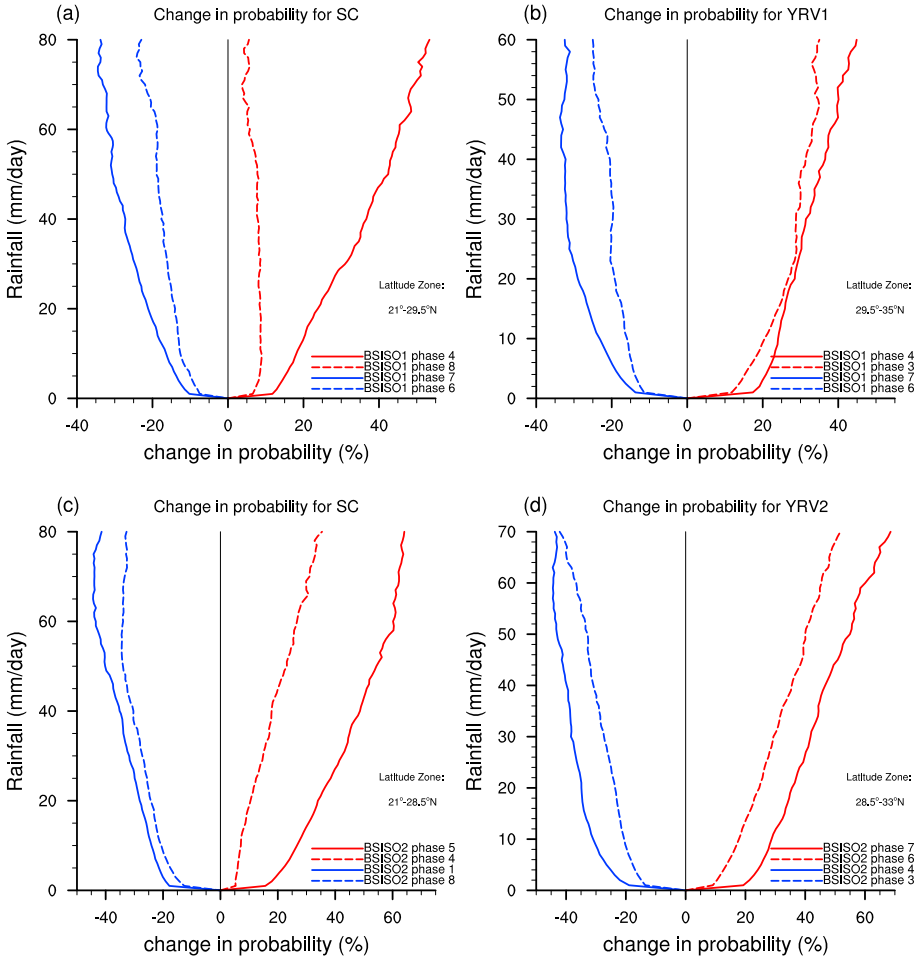

Figure 6. (a and b) Percentage changes in the probability of rainfall for typical active phases (red lines) and typical suppressed phases (blue lines) of boreal summer intraseasonal oscillation 1 with respect to the probability-distribution function of all May–August days. (c and d) The same as (a) and (b) but for boreal summer intraseasonal oscillation 2 phases.

there is a northward propagation in the impacts of BSISO2 on extreme rainfall. Phases 4 and 5 of BSISO2 have a more positively distribution relative to the PDFs for all MJJA days in SC. Along with the northward propagation of BSISO2, the rainfall becomes more positively skewed in YRV2 during phases 6 and 7. In a brief summary, during phases 4 and 8 and phases 3 and 4 of BSISO1, the extreme rainfall is in active phases, respectively, for SC and YRV1, whereas phases 6 and 7 are suppressed phases of extreme rainfall for SEC region. Similarly, the BSISO2 phases 4 and 5 and phases 6 and 7 are typical active phases of extreme rainfall for SC and YRV2, respectively. The corresponding suppressed phases for SC and YRV2 are phases 1 and 8 and phases 3 and 4, respectively.

These differences are further illustrated in Figure 6 as percentage changes in rainfall PDFs averaged in specific areas during the typical active phases (red lines) and typical suppressed phases (blue lines). It can be clearly seen that the probabilities of rainfall are substantially higher during typical active phases than during typical suppressed phases for both BSISO1 (Figures 6a and 6b) and BSISO2 (Figures 6c and 6d). Moreover, we can see that the more extreme the rainfall is, the more the probability increases due to the modulations of typical phases of the BSISO. From Figures 6a and 6b, the probability of rainfall over 60 mm/d increases more than 40% during the phase 4 of BSISO1 in SC. Phases 3 and 4 of BSISO1, as typical active phases for the occurrence of extreme rainfall in YRV1, can increase the probabilities of rainfall exceeding 50 mm/d by about 35%. From Figures 6c and 6d, we can see that the probabilities of rainfall exceeding 60 mm/d increase more than 60% during the phase 5 of BSISO2 in SC and the phase 7 of BSISO2 in YRV2.

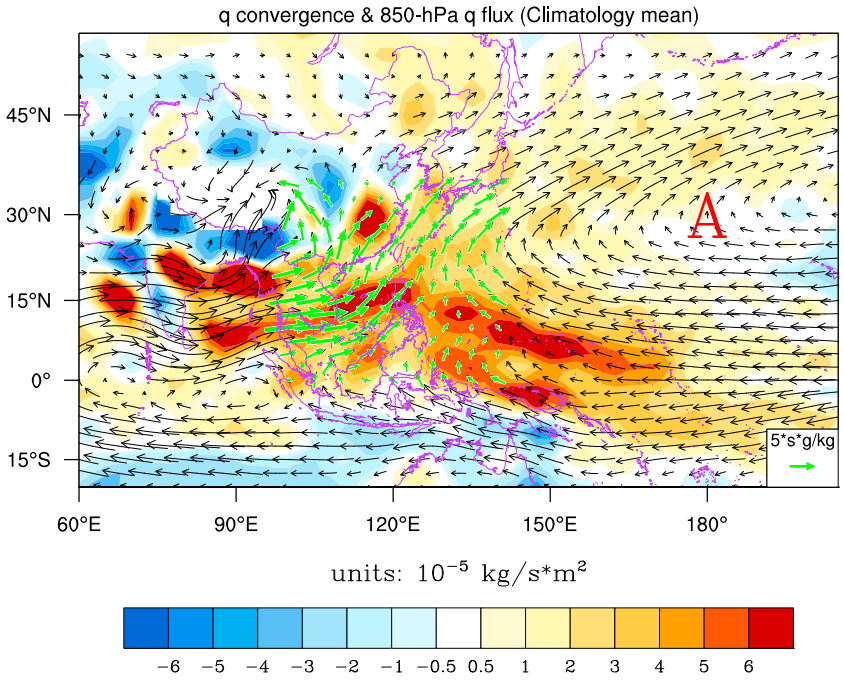

Figure 7. Climatological mean of column-integrated moisture convergence (shading, positive is convergence and negative is divergence, unit: 10^{-5} kg/s * m^2) and 850-hPa moisture flux (vector, unit: 5 * s * g/kg) for May–August. Letter "A" represents the anticyclonic circulation.

3.2. Physical Basis of Extreme Rainfall Changes

Several studies have suggested that the changes in upward motion and moisture are directly related to extreme rainfall changes (Loriaux et al., 2016; O'Gorman & Schneider, 2009). To better understand the moisture processes with the occurrence of the extreme rainfall, we have examined the moisture flux divergence ($\frac{1}{g}\nabla\cdot\left(q\vec{V}\right)$), which is considered as an important factor of heavy rainfall during BSISO1 phases and BSISO2 phases. The complete equation of moisture flux divergence is listed as follows:

$$\frac{1}{g}\nabla\cdot\left(q\vec{V}\right)=\frac{1}{g}\vec{V}\cdot\nabla q+\frac{1}{g}q\nabla\cdot\vec{V} \tag{2}$$

Moisture flux divergence includes two items, one is the moisture advection and the other is the moisture convergence. The moisture advection was not considered in our study because its contribution to extreme rainfall is negligible (Hsu et al., 2016; Ren & Ren, 2017).

First, the climatological mean moisture convergence and 850-hPa moisture flux are shown in Figure 7. In boreal summer, there are three major water vapor channels that transport moisture to SEC. They are the southwesterly moisture transport from the Bay of Bengal, the southerly moisture transport from the SC Sea, and the southeasterly moisture transport from the Western North Pacific (WNP). Rich moisture supply makes abundant rainfall in the SEC possible.

Then, the composites of moisture anomalies during BSISO1 phases 1–8 with respect to the seasonal mean are given in Figure 8. It can be seen that the spatial distribution of moisture convergence anomalies in the SEC is considerably modulated by BSISO1 life cycle. In phases 1–2 of BSISO1 (Figures 8a and 8b), corresponding to anticyclonic anomaly over the Philippine Sea and SC Sea, abnormal moisture divergence at western part of anticyclone induces an unfavorable condition for the occurrence of extreme events in Hainan Island. In the following two phases (Figures 8c and 8d), the anticyclonic anomalies move to the WNP and change to be northeast-southwest oriented, and the YRV is dominated by westerly anomalies located in the northwest side of the anomalous anticyclone. This configuration of circulation facilitates the transport of moisture to the YRV and induces significant moisture convergence there. Meanwhile, the BSISO1-related cyclonic anomalies propagate northeastward into Bay of Bengal and Indian Subcontinent in phases 4 and 5 (Figures 8d and 8e),

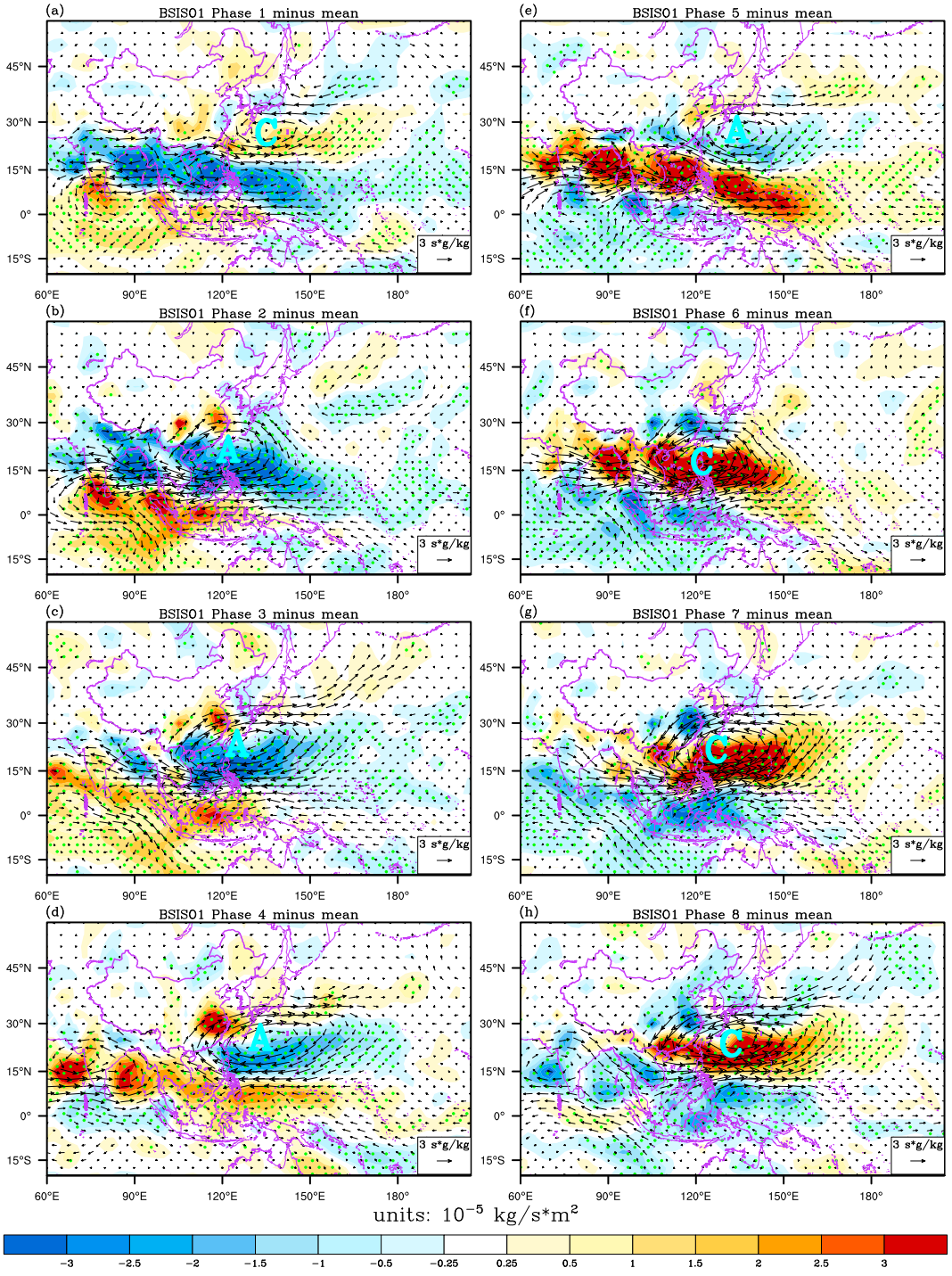

Figure 8. Changes of moisture convergence (shading) and 850-hPa moisture flux (vector) in boreal summer intraseasonal oscillation 1 phases 1–8 relative to climatological mean (Figure 7). Changes in moisture convergence exceeding the 95% confidence level based on a Student's *t* test are dotted in green. Letters "A" and "C" represent the anticyclonic anomalies and cyclonic anomalies, respectively.

which induce significant moisture convergence in Hainan. When the cyclonic anomalies propagate northeastward into the Philippine Sea and SC Sea during phases 6 and 7 of BSISO1 (Figures 8f and 8g), anomalous northeasterly is unfavorable for moisture convergence in the SEC region. As BSISO1 further moves to the northeast during phase 8 (Figure 8h), the associated westerly induces significant moisture convergence in SC.

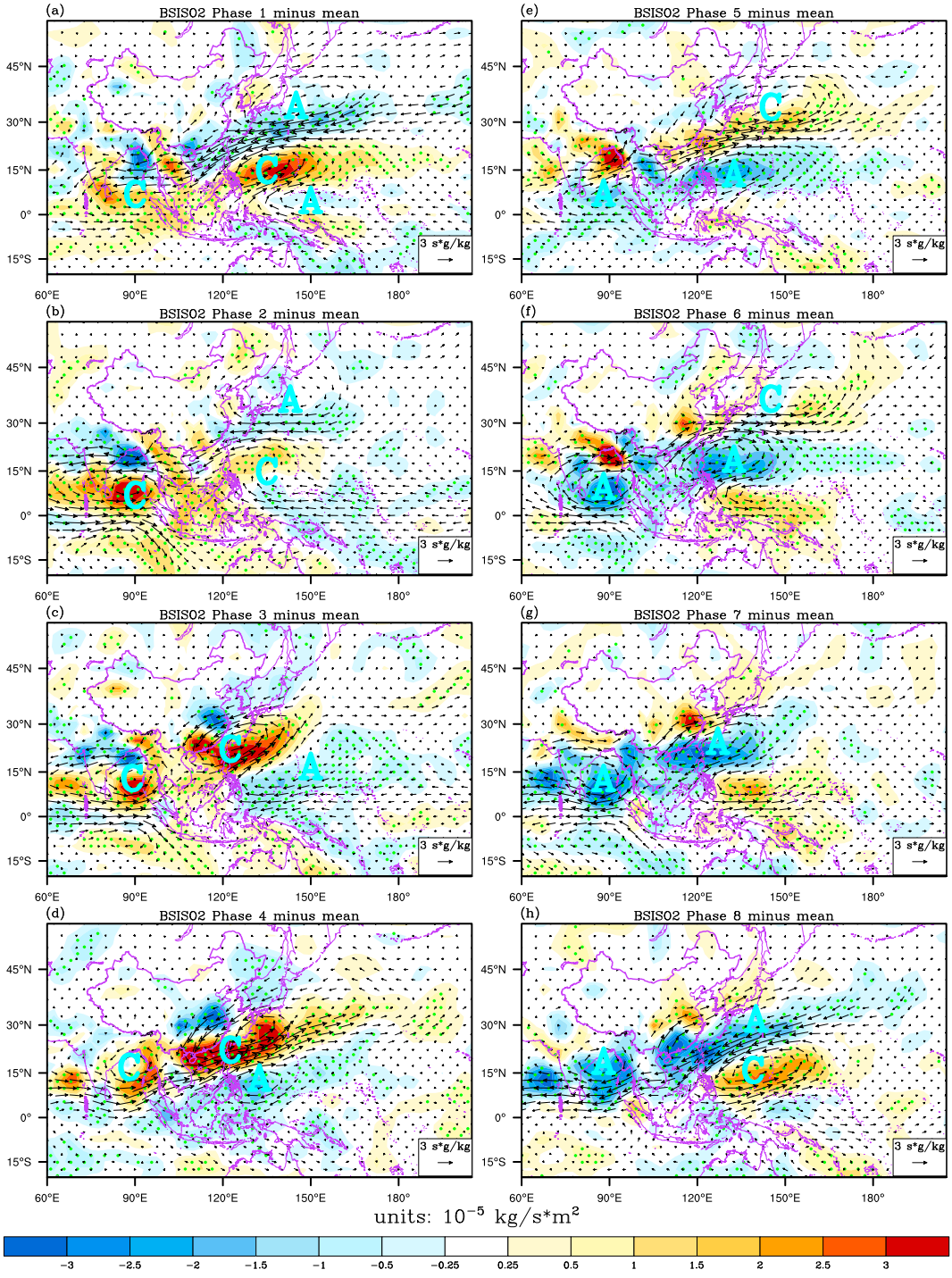

Figure 9. Same as Figure 8 but for phases 1–8 of boreal summer intraseasonal oscillation 2, respectively.

Boreal summer intraseasonal oscillation 2 variability also exerts significant influences on extreme rainfall in the SEC region via modulating the atmospheric moisture convergence. During phases 1 and 8 of BSISO2 (Figures 9h and 9a), corresponding to a strong anomalous anticyclone near Japan and a strong anomalous cyclone over the Philippine Sea, associated northeasterly induces significant moisture divergence in the SC. As BSISO2 propagates northwestward, the associated anomalous cyclone moves slowly close to the coastal areas of SEC during phases 3–5 (Figures 9c–9e); this is beneficial to the moisture convergence in

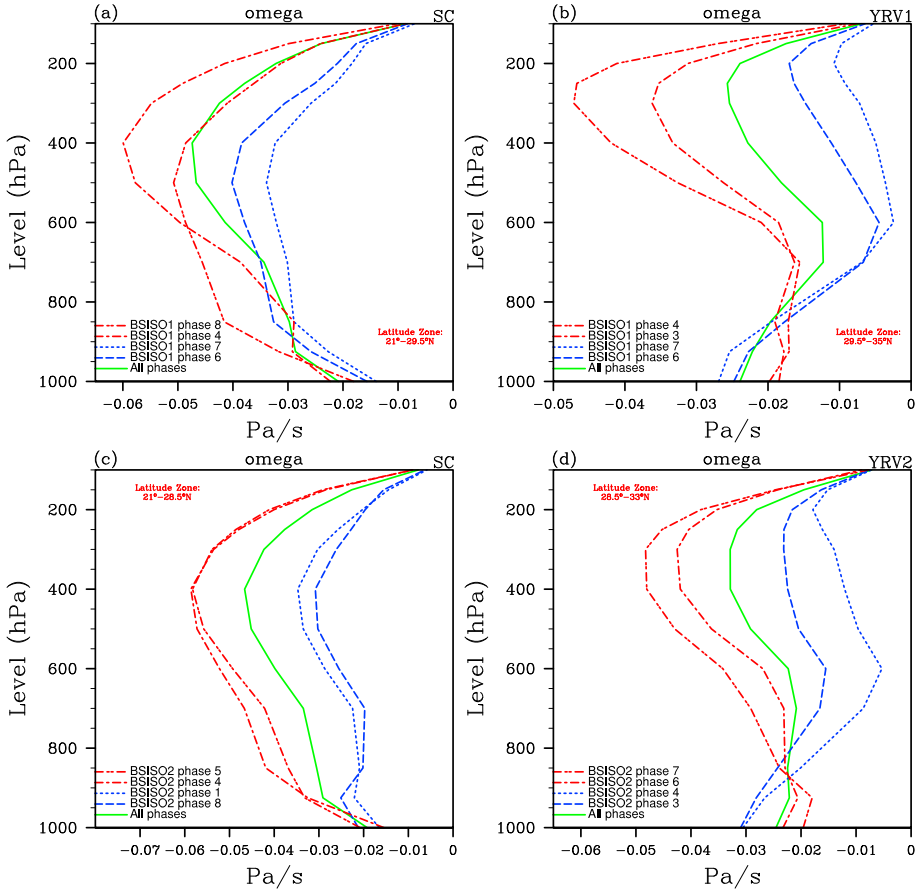

Figure 10. Composite profiles of vertical pressure velocity. Climatological values are shown in green, typical active phases of boreal summer intraseasonal oscillation 1 (or boreal summer intraseasonal oscillation 2) in red, and typical suppressed phases in blue.

the SC. At the same time, the YRV is still controlled by the northeasterly. Therefore, the BSISO2 phases 3–5 provide a favorable condition for the occurrence of extreme rainfall in SC but not in the YRV. As BSISO2 further moves to the northwest, the SEC region is gradually controlled by an anticyclone. The associated southwesterly transports abundant water vapor to YRV, which favors the occurrence of extreme rainfall there during phases 6 and 7 (Figures 9f and 9g). On the northward course of BSISO2 (phases 4–8), the associated anomalous anticyclone also moves northwestward from Philippine Sea to the Japan Sea, which results in a northward progression of moisture convergence (Figures 9d–9h) and regions with increased extreme rainfall (Figure 4).

In order to further demonstrate the contributions of upward motion and vertical moisture transport to rainfall extremes, Figures 10 and 11 show the mean profiles of vertical pressure velocity (ω) and vertical moisture advection ($-\omega\frac{\partial q}{\partial p}$), which are supposed to be related to extreme rainfall (Loriaux et al., 2016). Figure 10 shows the vertical velocity profiles, which are closely related to large-scale convergence. For the BSISO1, the upward motions in SC and YRV1 are systematically intensified during phases 4 and 8 and phases 3 and 4, respectively. For the BSISO2, the ascending motions in the SC and YRV2 are much stronger during phases 4 and 5 and phases 6 and 7, respectively. On the contrary, the upward motions at a specific area are consistently reduced during the typical suppressed phases of BSISO1 (or BSISO2). Similarly, the profiles of vertical moisture advection are given in Figure 11. Along with the changes in vertical motion, we can clearly see that the vertical moisture advection at middle and upper levels is substantially enhanced during typical active phases of BSISO1 (or BSISO2). It is expected that the associated moisture detrainment at midlevels makes the environment more favorable for further convection development. The clear separations of large-scale vertical velocity and moisture advection profiles between typical active and suppressed phases further testify the

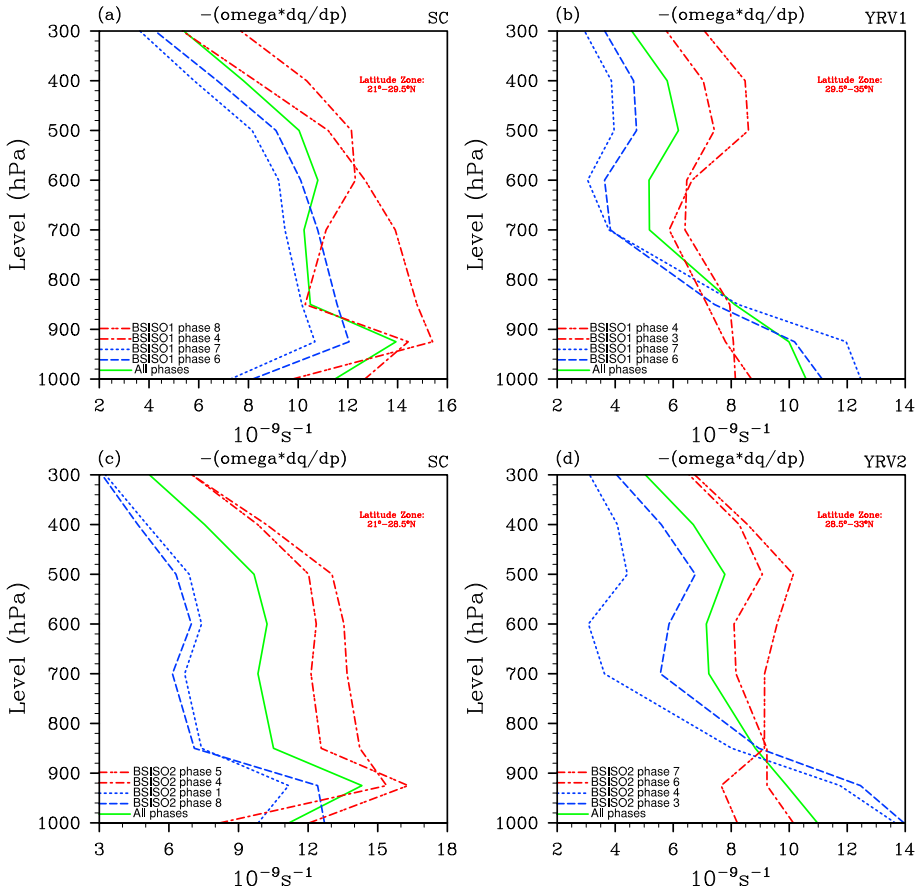

Figure 11. Same as Figure 10 but for the composite of vertical moisture advection.

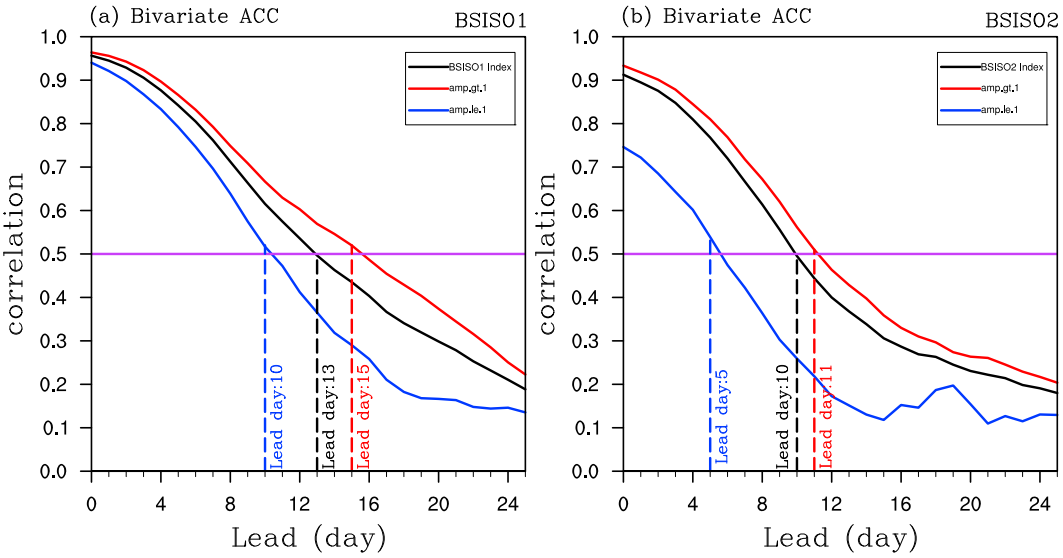

Figure 12. Correlation skill for the bivariate (a) BSISO1 and (b) BSISO2 indices between Climate Forecast System version 2 and observation's counterpart as a function of lead days. The black curves, the red curves, and the blue curves represent boreal summer intraseasonal oscillation (BSISO) indices, strong BSISOs, and weak BSISOs, respectively.

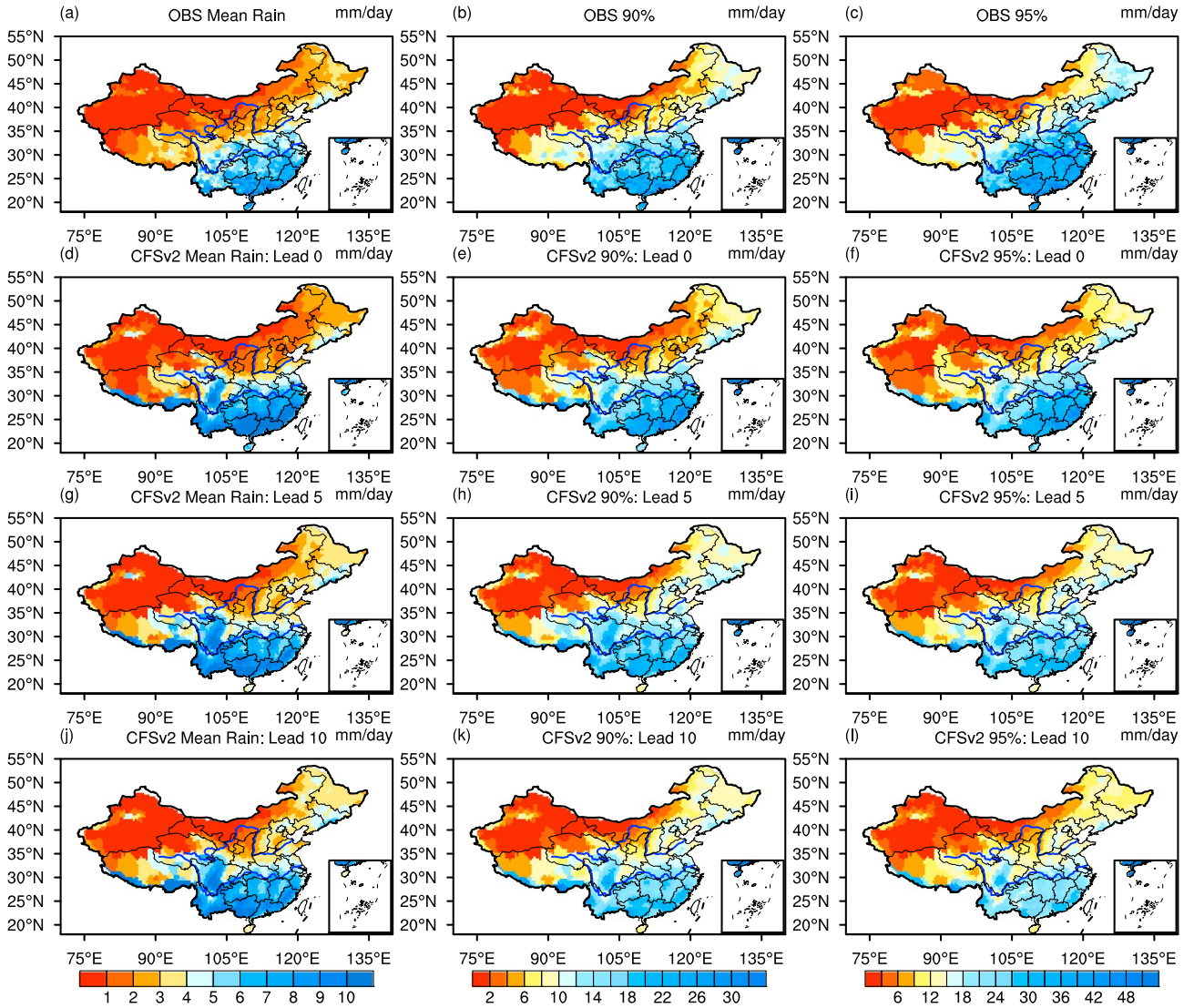

Figure 13. (a–c) Mean rainfall and 90th and 95th percentile values of rainfall (mm/d) in observations are compared with (d–f) those from Climate Forecast System version 2forecasts at lead day 0, (g–i) for lead day 5, and (j–l) for lead day 10.

strong modulations of BSISO on extreme rainfall. During the active (suppressed) phases, the intensified (weakened) large-scale upward motion and moisture advection apparently favors the increased (decreased) probability of the extreme rainfall.

4. Predictability of Extreme Rainfall in CFSv2

Another goal of this study is to evaluate CFSv2's capability of reproducing the BSISO's influences on extreme rainfall probability. Liu and Wang (2015) have shown that the intraseasonal forecast skill of rainfall in CFSv2 tends to be higher when the amplitudes of the MJO and BSISO are lager, especially for the BSISO. Figure 12 shows the bivariate ACC of the CFSv2 BSISO1 (Figure 12a) and BSISO2 (Figure 12b) with the observationally based counterpart. Taken 0.5 as the threshold of useful ACC skill, the BSISO1 (BSISO2) can be predicted out to 13-day (10-day) lead time. The dependence of the forecast skill on the BSISOs amplitude suggests that the useful forecast skill of BSISO1 reaches about 15 (10) days when the BSISO1 amplitude was large (small). Similarly, the useful skill of BSISO2 reaches 11 (5) days for strong (weak) BSISO2 events. Present evaluation will further derive probabilistic information of extreme rainfall during the passage of BSISO. After

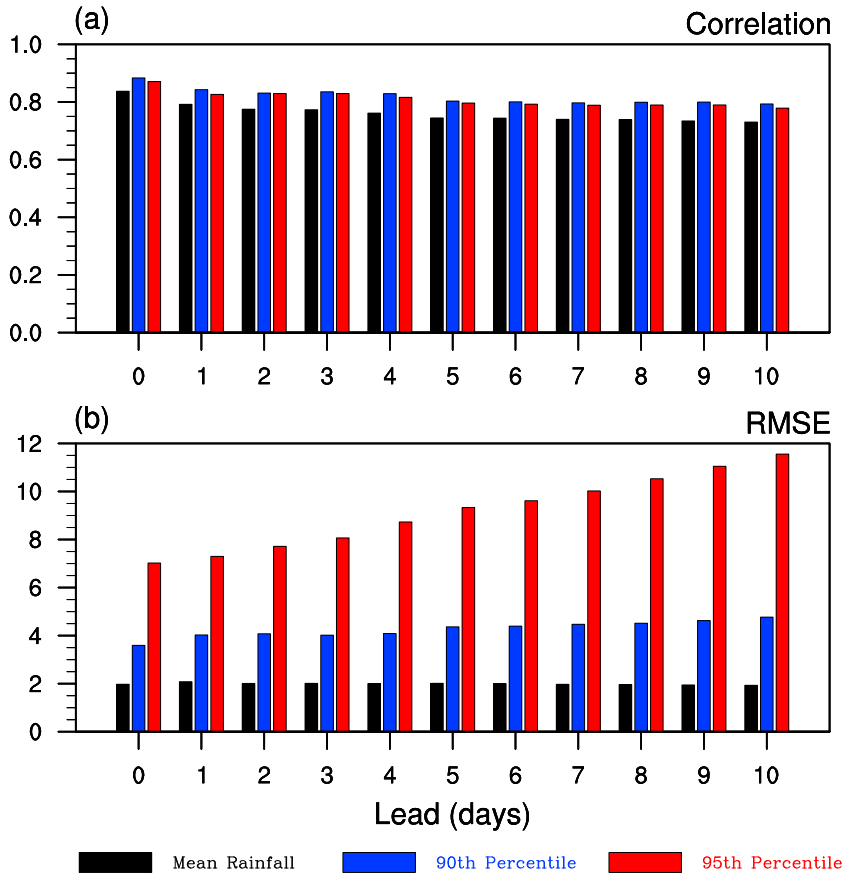

Figure 14. (a) Pattern correlation and b root-mean-square error of the rainfall in Figure 13 between observations and Climate Forecast System version 2 forecasts from lead day 0 to day 10.

interpolating onto the observational stations, the hindcast data of the CFSv2 during the period 1999–2010 are used for evaluation. The observational data during the same period have been used to verify the rainfall forecasts.

Figure 13 shows the spatial distributions of observational mean rainfall and the 90th and 95th percentile values and compares them with the CFSv2 forecasts at lead day 0, lead day 5, and lead day 10. We can see that the model strongly damps the amplitude of rainfall amounts, particularly for extreme rainfall, with the increase of lead time (e.g., lead day 10). Furthermore, the pattern correlation and root-mean-square error (RMSE) between observations and CFSv2 forecasts from lead day 0 to day 10 are shown in Figure 14. We can see that regardless of the average rainfall and the 90th and 95th percentile value, the correlation coefficient does not change much with the lead time and stays above 0.7. Which means the spatial patterns, center locations, and the decreasing trend from southeastern to northwestern China of average rainfall and extreme values can be well captured and represented with high skill by the model. However, we all know that correlation analysis only reflects the correlation between two variables, which is insensitive to the amplitude error between variables. The RMSE can take into account errors in amplitude, which is also shown in Figure 14. We can clearly see that RMSE increases with the increase of the lead time and the amount of rainfall. This proved in another way that the amplitude of rainfall, especially extreme rainfall, decreases with the increase of the CFSv2 lead time. Therefore, in order to avoid the weakening of the amplitude of extreme rainfall in the CFSv2, we used the respective percentile values of the observation and model in the subsequent study. The ability of the model in forecasting the probability changes of regional extremes is further examined in Figures 15 and 16, which show the percentage changes in the probability of percentile rainfall with the forecasts initialized from phases 1–8 of BSISO1 and BSISO2, respectively. We can see that, within 2 weeks, the CFSv2 is able to capture the observed probability increases of extreme rainfall in the SC and YRV1 during phases 1 and 8 and the phases 2 and 3 as well as the suppression of extreme rainfall in SC and YRV1

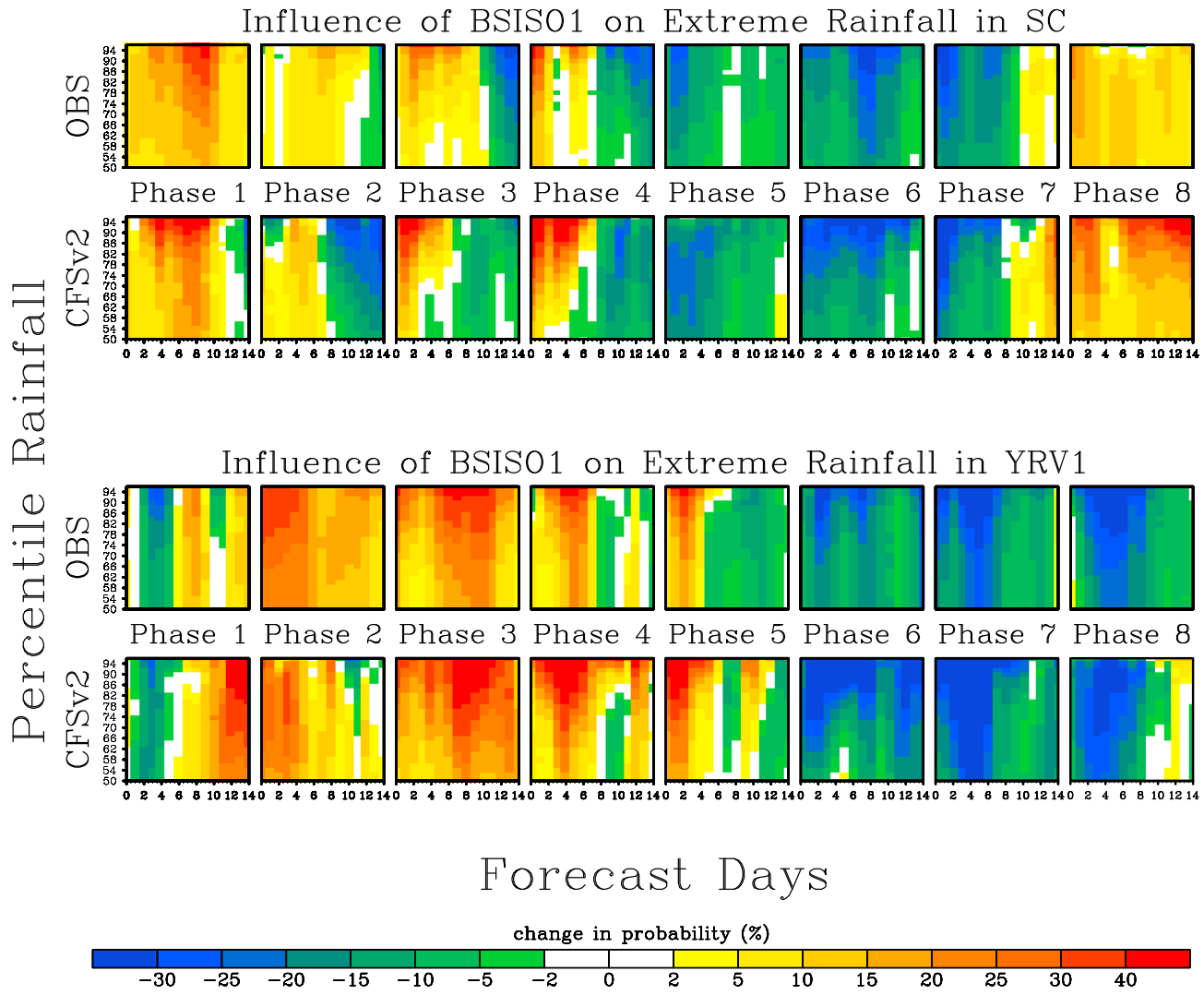

Figure 15. Percentage changes in the probability of rainfall as a function of forecast time (day) when initialized from phases 1–8 of boreal summer intraseasonal oscillation 1 with respect to a climatological probability-distribution function, where the upper two rows represent South China and bottom two rows for Yangtze River Valley 1.

during phases 5 and 6 and phases 6 and 7 of BSISO1, respectively. General agreements between model forecasts and observations indicate that the CFSv2 is able to reproduce the modulations of BSISO1 on extreme rainfall at least for lead time of 2 weeks. Similarly, the CFSv2 system's ability for reproducing the influences of BSISO2 on extreme rainfall is also examined in Figure 16. The results from Figure 16 show that the CFSv2 model has good skill to predict the BSISO2's impacts on extreme rainfall in 2 weeks. We also notice that the predictability of extreme rainfall in the SC is better than YRV2, which may be due to the YRV2 being away from the main convection region of BSISO2. When the modulations of the BSISO2 weaken, the CFSv2's forecasting skill of extreme rainfall is also reduced. Furthermore, in order to quantitatively evaluate the predictability of CFSv2 for forecasting extreme rainfall, we have calculated the pattern correlation (Figure 17) of percentage change between the CFSv2 and observations in Figures 15 and 16. From the results of correlation analysis, we can see that the CFSv2 model has a good predictive ability for the continuous change of extreme rainfall probability. Except for the individual phases (such as BSISO2 phase 5 relative to YRV2) that did not pass the significance test, CFSv2 can effectively predict the probability anomalies of rainfall in SEC within 2 weeks. The above encouraging results show that the CFSv2 system can be used to make extended-range predictions for the probabilistic information of extreme rainfall based on the BSISO's impacts in SEC region.

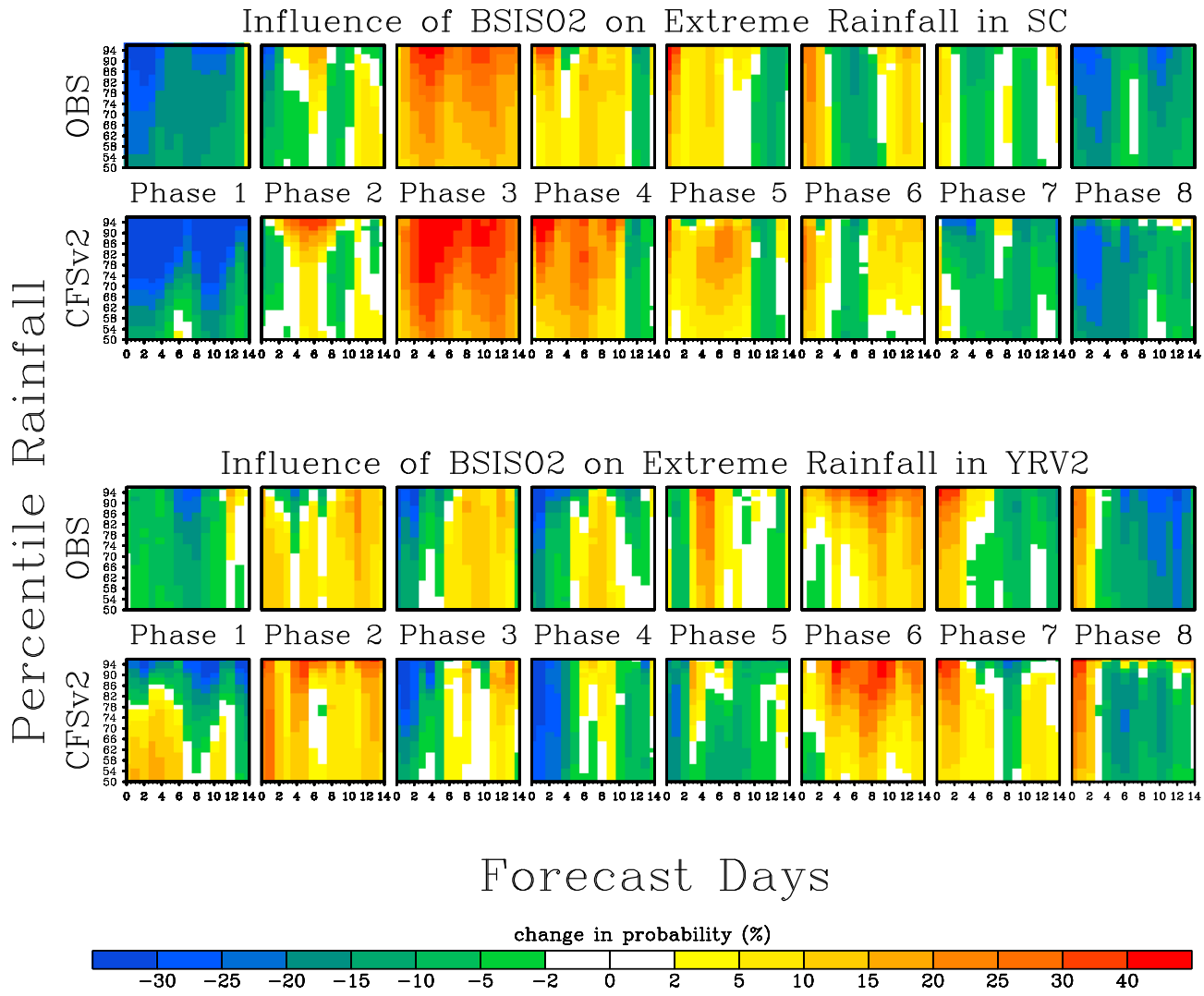

Figure 16. Same as Figure 15 but initialized from phases 1–8 of boreal summer intraseasonal oscillation 2, where the upper two rows represent South China and bottom two rows for Yangtze River Valley 2.

5. Summary and Discussion

This study documented the statistical relationships between the BSISO and the probabilities and spatial distributions of extreme rainfall in the EC, particularly in the SEC region. The associated atmospheric circulations and moisture processes were analyzed to reveal the physical mechanisms through which the BSISO modulates the occurrence of extreme rainfall. Finally, the CFSv2's ability to capture the observed relationships was evaluated, and its probabilistic predictability of extreme rainfall in the SEC at medium-to-extended range was assessed.

We found that the responses of extreme rainfall to BSISO activity in the EC are not uniform. Based on the distinctive impacts of BSISO1 on extreme rainfall, the SEC can be divided into two subregions: SC (21°N–29.5°N) and YRV1 (29.5°N–35°N). Similarly, the SEC can be divided into two subregions: SC (21°N–28.5°N) and YRV2 (28.5°N–33°N) based on the impacts of BSISO2. The BSISO1 significantly increases the probabilities of extreme rainfall by about 35–45% for SC and YRV1, respectively, during phases 4 and 8, and phases 3–4, showing a southward propagation with the speed of 1.96°/phase. The BSISO2, however, increases the probability of rainfall extremes by more than 40% in the SC and YRV2, respectively, during phases 4 and 5 and phases 6 and 7. This is due to the changes in skewness of rainfall PDF along with the life cycle of BSISO. During the typical active phases, regional rainfall PDF skews toward larger values compared

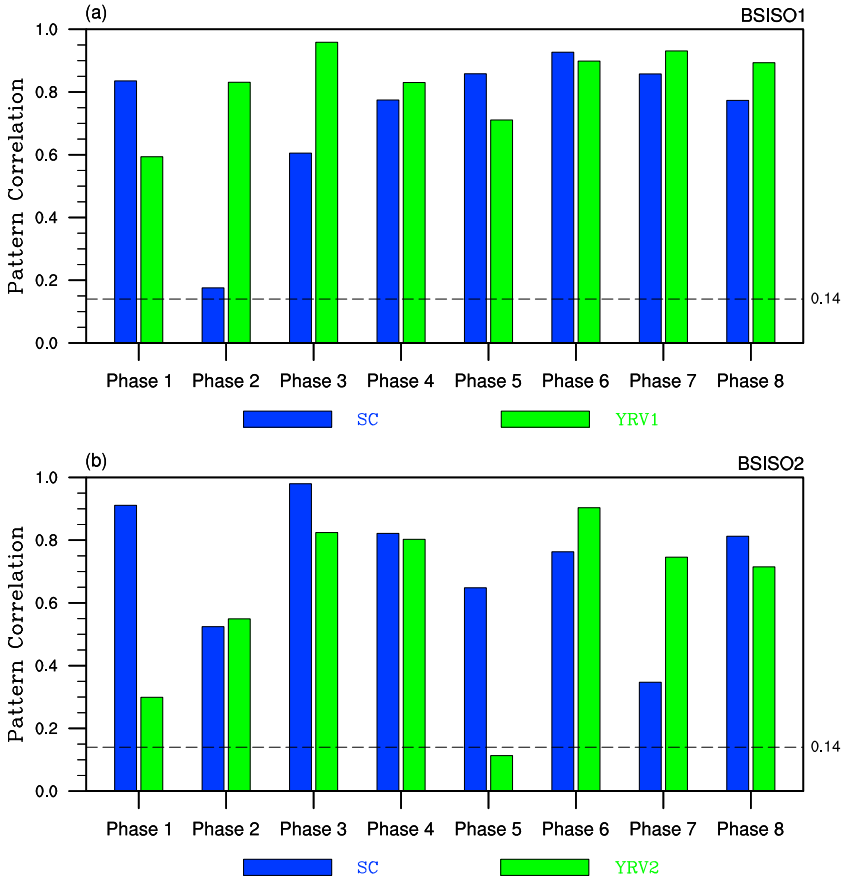

Figure 17. (a) Pattern correlations of percentage change between the Climate Forecast System version 2 and observations in Figure 15, during the phases 1–8 of boreal summer intraseasonal oscillation 1. B is the same as a but for the pattern correlations in Figure 16, during the phases 1–8 of boreal summer intraseasonal oscillation 2. The black dotted line corresponds to the correlation of 99% confidence level.

with all-day PDF. It is further noticed that, as a response to the 10 to 30-day northwestward-propagating BSISO mode (Figure 9), the region with significant increases in 90th extremes during phases 4–7 of BSISO2 also exhibits a steady northward progression with a speed of 2.75°/phase (Figure 4).

The BSISO influences the extreme rainfall in the SEC mainly through changing the large-scale atmospheric circulations and moisture supplies from the Bay of Bengal, the SC Sea, and WNP. During its life cycle, the associated circulation and moisture changes will induce large-scale moisture convergence in a specific area of SEC. The moisture convergence further leads to intensified upward motion and vertical moisture advection, thus providing a more favorable condition for the occurrence of extreme rainfall. Our analyses corroborate that both horizontal moisture convergence and vertical moisture advection can serve as key factors of extreme-rainfall events.

Extended-range hindcasts of CFSv2 during 1999–2010 have been used to evaluate the model's capability in representing the BSISO's impacts on rainfall extremes. It is revealed that the BSISO1 (BSISO2) can be predicted out to 13-day (10-day) lead time by CFSv2. Besides, the model is able to capture the observed spatial patterns of climatological rainfall, extreme values at 90th and 95th percentiles in the SEC. Within 2 weeks, CFSv2 can largely reproduce the observed impacts of BSISO on extreme rainfall. This result suggests that CFSv2 has great potential for monitoring and forecasting the probabilistic information of extreme rainfall in the SEC based on real-time BSISO indices.

Current study focused on the effects of BSISO on extreme rainfall in the SEC. Other studies (e.g., Jeong et al., 2005) also found that the spatial pattern and magnitude of surface air temperature anomalies over East Asia vary significantly with MJO phases in boreal winter. Whether and how the BSISO modes influence the surface air temperature extremes in the EC deserve further study. Besides, current study shows that both horizontal

moisture convergence and vertical moisture advection can provide more favorable conditions for the occurrence of extreme rainfall under the influence of BSISOs. However, it should be noted that the local vertical velocity and vertical moisture advection can also be caused by rainfall extremes themselves since rainfall-caused diabatic heating will have a feedback on the atmospheric circulations (Lu & Lin, 2009). Therefore, the physical mechanism of BSISOs increasing the probability of extreme rainfall remains to be further studied.

Acknowledgments
The daily rainfall from 2,400 stations in China was provided by the National Meteorological Information Center of the China Meteorological Administration (http://data.cma.cn/). The atmospheric circulation data used in this work came from NCEP/NCAR Reanalysis data (https://www.esrl.noaa.gov/psd/data/gridded/data.ncep.reanalysis.pressure.html). The CFSv2 hindcasts are available at the National Oceanic and Atmospheric Administration (https://www.ncdc.noaa.gov/data-access/model-data/model-datasets/climate-forecast-system-version2-cfsv2). This work was jointly supported by the National Basic Research (973) Program of China under grant 2015CB453203; the National Key Research Program and Development of China (2017YFC1502302); the China Meteorological Special Project under grant GHY201406022; the China National Sciences Foundation under grants 41505065, 41375062, and 41775066; and the 973 Program of China under grant 2010CB950404.

References

Alvarez, M. S., Vera, C. S., Kiladis, G. N., & Liebmann, B. (2016). Influence of the Madden Julian Oscillation on precipitation and surface air temperature in South America. *Climate Dynamics*, *46*(1–2), 245–262. https://doi.org/10.1007/s00382-015-2581-6

Barlow, M., Wheeler, M., Lyon, B., & Cullen, H. (2005). Modulation of daily precipitation over southwest Asia by the Madden-Julian oscillation. *Monthly Weather Review*, *133*(12), 3579–3594. https://doi.org/10.1175/Mwr3026.1

Bond, N. A., & Vecchi, G. A. (2003). The influence of the Madden-Julian Oscillation on precipitation in Oregon and Washington. *Weather and Forecasting*, *18*(4), 600–613. https://doi.org/10.1175/1520-0434(2003)018%3C0600:tiotmo%3E2.0.co;2

Chen, J., Wen, Z., Wu, R., Chen, Z., & Zhao, P. (2015). Influences of northward propagating 25–90-day and quasi-biweekly oscillations on eastern China summer rainfall. *Climate Dynamics*, *45*(1–2), 105–124. https://doi.org/10.1007/s00382-014-2334-y

Fu, X., Lee, J. Y., Wang, B., Wang, W., & Vitart, F. (2013). Intraseasonal forecasting of the Asian summer monsoon in four operational and research models. *Journal of Climate*, *26*(12), 4186–4203. https://doi.org/10.1175/jcli-d-12-00252.1

Gao, J., Chen, C., Zhou, X., & You, L. (2013). Analysis of low-frequency features on typical persistent heavy rainfall during pre-flood season in Fujian Province in 2010 (in Chinese). *Advances in Meteorological Science and Technology*, *3*(1), 39–45. https://doi.org/10.3969/j.issn.2095-1973.2013.01.006

Hsu, P. C., Lee, J. Y., & Ha, K. J. (2016). Influence of boreal summer intraseasonal oscillation on rainfall extremes in southern China. *International Journal of Climatology*, *36*(3), 1403–1412. https://doi.org/10.1002/joc.4433

Huang, R., Xu, Y., Wang, P., & Zhou, L. (1998). The features of the catastrophic flood over the Changjiang River basin during the summer of 1998 and cause exploration (in Chinese). *Climatic and Environmental Research*, *3*(04), 300–313. https://doi.org/10.3878/j.issn.1006-9585.1998.04.02

Jeong, J. H., Ho, C. H., Kim, B. M., & Kwon, W. T. (2005). Influence of the Madden-Julian Oscillation on wintertime surface air temperature and cold surges in East Asia. *Journal of Geophysical Research*, *110*, D11104. https://doi.org/10.1029/2004JD005408

Jia, X., Chen, L., Ren, F., & Li, C. (2011). Impacts of the MJO on winter rainfall and circulation in China. *Advances in Atmosphere Sciences*, *28*(3), 521–533. https://doi.org/10.1007/s00376-010-9118-z

Jiang, X., Li, T., & Wang, B. (2004). Structures and mechanisms of the northward propagating boreal summer intraseasonal oscillation. *Journal of Climate*, *17*(5), 1022–1039. https://doi.org/10.1175/1520-0442(2004)017%3C1022:samotn%3E2.0.co;2

Jones, C. (2000). Occurrence of extreme precipitation events in California and relationships with the Madden-Julian Oscillation. *Journal of Climate*, *13*(20), 3576–3587. https://doi.org/10.1175/1520-0442(2000)013%3C3576:ooepei%3E2.0.co;2

Jones, C., Waliser, D. E., Lau, K. M., & Stern, W. (2004). Global occurrences of extreme precipitation and the Madden-Julian Oscillation: Observations and predictability. *Journal of Climate*, *17*(23), 4575–4589. https://doi.org/10.1175/3238.1

Kalnay, E., Kanamitsu, M., Kistler, R., Collins, W., Deaven, D., Gandin, L., et al. (1996). NCEP/NCAR 40-year reanalysis project. *Bulletin of the American Meteorological Society*, *77*(3), 437–472. https://doi.org/10.1175/1520-0477(1996)077%3C0437:TNYRP%3E2.0.CO;2

Lee, J.-Y., Wang, B., Wheeler, M. C., Fu, X., Waliser, D. E., & Kang, I.-S. (2012). Real-time multivariate indices for the boreal summer intraseasonal oscillation over the Asian summer monsoon region. *Climate Dynamics*, *40*(1–2), 493–509. https://doi.org/10.1007/s00382-012-1544-4

Lee, S.-S., Moon, J.-Y., Wang, B., & Kim, H.-J. (2017). Subseasonal prediction of extreme precipitation over Asia: Boreal summer intraseasonal oscillation perspective. *Journal of Climate*, *30*(8), 2849–2865. https://doi.org/10.1175/jcli-d-16-0206.1

Lee, S.-S., Wang, B., Waliser, D. E., Neena, J. M., & Lee, J. Y. (2015). Predictability and prediction skill of the boreal summer intraseasonal oscillation in the Intraseasonal Variability Hindcast Experiment. *Climate Dynamics*, *45*(7–8), 2123–2135. https://doi.org/10.1007/s00382-014-2461-5

Ling, J., Bauer, P., Bechtold, P., Beljaars, A., Forbes, R., Vitart, F., et al. (2014). Global versus local MJO forecast skill of the ECMWF model during DYNAMO. *Monthly Weather Review*, *142*(6), 2228–2247. https://doi.org/10.1175/mwr-d-13-00292.1

Liu, R.-F., & Wang, W. (2015). Multi-week prediction of South-East Asia rainfall variability during boreal summer in CFSv2. *Climate Dynamics*, *45*(1–2), 493–509. https://doi.org/10.1007/s00382-014-2401-4

Loriaux, J., Lenderink, G., & Siebesma, A. P. (2016). Peak precipitation intensity in relation to atmospheric conditions and large-scale forcing at midlatitudes. *Journal of Geophysical Research: Atmospheres*, *121*, 5471–5487. https://doi.org/10.1002/2015jd024274

Lu, R. Y., & Lin, Z. D. (2009). Role of subtropical precipitation anomalies in maintaining summertime meridional teleconnections over the western North Pacific and East Asia. *Journal of Climate*, *22*(8), 2058–2072. https://doi.org/10.1175/2008JCLI2444.1

Madden, R. A., & Julian, P. R. (1971). Detection of a 40–50 day oscillation in the zonal wind in the tropical Pacific. *Journal of the Atmosphere Sciences*, *28*(5), 702–708. https://doi.org/10.1175/1520-0469(1971)028%3C0702:doadoi%3E2.0.co;2

Madden, R. A., & Julian, P. R. (1972). Description of global-scale circulation cells in the tropics with a 40–50 day period. *Journal of the Atmosphere Sciences*, *29*(6), 1109–1123. https://doi.org/10.1175/1520-0469(1972)029%3C1109:dogscc%3E2.0.co;2

Madden, R. A., & Julian, P. R. (1994). Observations of the 40–50-day tropical oscillation—A review. *Monthly Weather Review*, *122*(5), 814–837. https://doi.org/10.1175/1520-0493(1994)122%3C0814:ootdto%3E2.0.co;2

Mao, J., & Wu, G. (2006). Intraseasonal variations of the Yangtze rainfall and its related atmospheric circulation features during the 1991 summer. *Climate Dynamics*, *27*(7–8), 815–830. https://doi.org/10.1007/s00382-006-0164-2

O'Gorman, P. A., & Schneider, T. (2009). The physical basis for increases in precipitation extremes in simulations of 21st-century climate change. *Proceedings of the National Academy of Sciences of the United States of America*, *106*(35), 14,773–14,777. https://doi.org/10.1073/pnas.0907610106

Ren, H.-L., & Ren, P. (2017). Impact of Madden-Julian Oscillation upon winter extreme rainfall in Southern China: Observations and predictability in CFSv2. *Atmosphere*, *8*(12), 192. https://doi.org/10.3390/atmos8100192

Saha, S., Moorthi, S., Pan, H. L., Wu, X. R., Wang, J. D., Nadiga, S., et al. (2010). The NCEP climate forecast system reanalysis. *Bulletin of the American Meteorological Society*, *91*(8), 1015–1058. https://doi.org/10.1175/2010BAMS3001.1

Saha, S., Moorthi, S., Wu, X. R., Wang, J., Nadiga, S., Tripp, P., et al. (2014). The NCEP climate forecast system version 2. *Journal of Climate*, *27*(6), 2185–2208. https://doi.org/10.1175/Jcli-D-12-00823.1

Wang, B., & Rui, H. (1990). Synoptic climatology of transient tropical intraseasonal convection anomalies: 1975–1985. *Meteorology and Atmospheric Physics*, *44*(1–4), 43–61. https://doi.org/10.1007/bf01026810

Wang, D., Xia, R., & Liu, Y. (2011). A preliminary study of the flood causing rainstorm during the first rainy season in South China in 2008 (in Chinese). *Acta Meteorologica Sinica*, *69*(1), 137–148. https://doi.org/10.11676/qxxb2011.012

Webster, P. J., Jian, J., Hopson, T. M., Hoyos, C. D., Agudelo, P. A., Chang, H. R., et al. (2010). Extended-range probabilistic forecasts of Ganges and Brahmaputra floods in Bangladesh. *Bulletin of the American Meteorological Society*, *91*(11), 1493–1514. https://doi.org/10.1175/2010BAMS2911.1

Wheeler, M. C., & Hendon, H. H. (2004). An all-season real-time multivariate MJO index: Development of an index for monitoring and prediction. *Monthly Weather Review*, *132*, 1917–1932. https://doi.org/10.1175/1520-0493(2004)132%3C1917:Aarmmi%3E2.0.Co;2

Xavier, P., Rahmat, R., Cheong, W. K., & Wallace, E. (2014). Influence of Madden-Julian Oscillation on Southeast Asia rainfall extremes: Observations and predictability. *Geophysical Research Letters*, *41*, 4406–4412. https://doi.org/10.1002/2014gl060241

Yang, J., Wang, B., & Bao, Q. (2010). Biweekly and 21–30-day variations of the subtropical summer monsoon rainfall over the lower reach of the Yangtze River basin. *Journal of Climate*, *23*(5), 1146–1159. https://doi.org/10.1175/2009jcli3005.1

Zhang, C. D., & Dong, M. (2004). Seasonality in the Madden-Julian Oscillation. *Journal of Climate*, *17*(16), 3169–3180. https://doi.org/10.1175/1520-0442(2004)017%3C3169:Sitmo%3E2.0.Co;2

Zhang, L., Wang, B., & Zeng, Q. (2009). Impact of the Madden-Julian Oscillation on summer rainfall in Southeast China. *Journal of Climate*, *22*(2), 201–216. https://doi.org/10.1175/2008jcli1959.1

Zhang, X. B., Alexander, L., Hegerl, G. C., Jones, P., Tank, A. K., Peterson, T. C., et al. (2011). Indices for monitoring changes in extremes based on daily temperature and precipitation data. *Wiley Interdisciplinary Reviews: Climate Change*, *2*(6), 851–870. https://doi.org/10.1002/wcc.147

Zhao, C., Zhou, T., Song, L., & Ren, H. (2014). The boreal summer intraseasonal oscillation simulated by four Chinese AGCMs participating in the CMIP5 project. *Advances in Atmospheric Sciences*, *31*(5), 1167–1180. https://doi.org/10.1007/s00376-014-3211-7

Zhu, C. W., Nakazawa, T., Li, J. P., & Chen, L. X. (2003). The 30–60 day intraseasonal oscillation over the western North Pacific Ocean and its impacts on summer flooding in China during 1998. *Geophysical Research Letters*, *30*(18), 1952. https://doi.org/10.1029/2003GL017817